

LETTER TO THE EDITOR

Strong clumping in global streaming instability simulations with a dusty fluid

Dominik Ostertag and Mario Flock

Max-Planck-Institut für Astronomie, Königstuhl 17, 69117 Heidelberg, Germany
e-mail: ostertag@mpia.de

January 31, 2025

ABSTRACT

Context. How planets form in protoplanetary disks and what drives the formation of their seeds is still a major unknown. It is an accepted theory that multiple processes can trap dusty material in radially narrow rings or vortex-like structures, preventing the dust from drifting inwards. However, the relevant process for clumping this dusty material until it collapses under gravity still needs to be identified. One promising candidate is the streaming instability arising from the aerodynamic interaction between dust and gas once they reach similar densities.

Aims. We investigate with a global disk model based on recent observational constraints if streaming instability can form dust clumps, which might gravitationally collapse. Further, our goal is to verify the observability of the produced structures using ALMA or ngVLA. *Methods.* For the first time, we present global 2D (R, z) hydrodynamic simulations using FARGO3D in which the dust is treated as a pressureless fluid. The disk model assumes stratification, realistic boundary conditions, and meaningful resolution to resolve the fast-growing modes. We choose two values for the total dust-to-gas mass ratio $Z = 0.01$ and $Z = 0.02$, compare the maximum clump density to the local Hill density, and compute the optical depth of the dust disk.

Results. With a dust-to-gas mass ratio of $Z = 0.01$, we confirm previous streaming instability simulations, not showing the ability to form strong concentrations of dust clumps. With $Z = 0.02$, dense clumps form within 20 orbits, however reaching only 30% of the Hill density even following disk parameters from the massive protoplanetary disks GM Aur, HD163296, IM Lup, MWC 480, and TW Hya, which all share an astonishing similar surface density profiles.

Conclusions. Our results show that clumping by the streaming instability to trigger self-gravity is less efficient than previously thought, especially when applying more realistic density profiles. By extrapolating our results, we estimate the gravitational collapse of concentrated pebbles earliest at 480 orbits, while for more frequent, less massive, or more compact disks, this time can reach 1000 orbits. Our results predict that substructures caused by streaming instability can vary between optical thin and optical thick at ALMA Band 1 wavelength for less massive disks. However, the average clump separation is 0.03 au at 10 au distance to the star, far too small to be observable with ALMA and even ngVLA. For the currently observed disks and best-fit surface density profiles, we predict efficient planetesimal formation outside 10 au, where the ratio of Hill- and gas midplane density is sufficiently small. Our results suggest that even for massive Class II disks, the critical Hill density can be reached in dust concentrations during 480 - 1000 orbits, corresponding to tens or hundreds of thousands of years, depending on the radial position.

1. Introduction

To properly study and understand the possible formation of planets and planetary seeds, it is crucial to understand the interplay between the gas and dust components within protoplanetary disks (Armitage & Kley 2019; Lesur et al. 2023). Small grains, which are well coupled to the gas, follow the gas structure, while larger grains are less coupled and settle towards the midplane. This natural behavior will then result in the accumulation of larger grains and, therefore, an increase in volumetric dust density, making it possible to have similar dust and gas densities. Because grains at the midplane are not completely decoupled from the gas, one needs to consider the aerodynamic drag effects from gas onto the dust and the impact of dust onto the gas because of similar densities. Many works have shown that these drag effects result in so-called drag instabilities (see, e.g., Squire & Hopkins 2018) where the streaming instability (Youdin & Goodman 2005) is one promising representative as it can lead to natural clumping of dust. This clumping can strongly increase the local dust density compared to the background dust disk (see Johansen et al. 2007, 2009, where this clumping was first described for a stratified disk in radial-azimuthal and radial-vertical direction, respectively). Studying this clumping effect

and its dependency on key disk parameters gains insights into the likelihood that streaming or other drag instabilities initiate the formation of planetesimals by the collapse of dense dust accumulations. Many works investigated the influence of the global dust-to-gas ratio (see also Johansen et al. 2009; Yang & Johansen 2014; Li & Youdin 2021), the gas pressure gradient (see, e.g. Sekiya & Onishi 2018; Abod et al. 2019), or external turbulence by considering additional disk instabilities (see, e.g. Schäfer et al. 2020; Schäfer & Johansen 2022) or by including forced turbulence (see, e.g. Gole et al. 2020; Lim et al. 2024a).

One common approach to studying streaming instability is using local shearing box simulations. However, to investigate the effect of streaming instability on planet formation, one needs to consider global simulations to give a clump enough time to drift inwards and collect more material. Flock & Mignone (2021) provided a model to study this instability with more realistic conditions for the gas pressure profile in a global stratified model and a reasonable resolution to resolve the fastest-growing modes using Lagrangian dust grains. In addition to modeling dust as individual particles, one can treat it as a pressure-less fluid if the Stokes number is below 0.1. See, e.g., Weber et al. (2019), Liu & Bai (2023), or Ziampras et al. (2024) for an incomplete list

of works that already use dust as a fluid. The work of [Kowalik et al. \(2013\)](#) studied streaming instability in an unstratified disk, treating dust as a pressureless fluid. To our knowledge, no work exists yet in which a global stratified protoplanetary disk was investigated, focusing on streaming instability and its influence on clump formation where the dust is modeled as a fluid. The structure of this work is as follows. Firstly, we will describe our used methods in Sect. 2. Then, in Sect. 3, we will simulate two disks with a dust-to-gas mass ratio of 1% and 2%, respectively. We finish this work with a discussion in Sect. 4 and a conclusion in 5.

2. Method and disk model

The setup of our disk model is the same as described in [Flock & Mignone \(2021\)](#) (see equations 1-10 therein). Therefore, we use spherical coordinates in radial and meridional direction (r, θ). To model dust as a pressure-less fluid, we use the publicly available hydrodynamics code FARGO3D (see [Benítez-Llambay & Masset 2016](#)) with the version to study one gas and potentially multiple dust species ([Benítez-Llambay et al. 2019](#)) including the effect of aerodynamic drag both from gas onto dust and from dust onto gas (often referred to as backreaction) and the implementation of dust diffusion (see [Weber et al. 2019](#)). The last public commit is from July 22nd, 2020. In Appendix B, we provide a detailed overview of applied damping and refilling techniques for both gas and dust. We set the spherical location of the inner (outer) damping zone to $r_{\text{inf}} = 9.349$ au ($r_{\text{sup}} = 10.643$ au). In the inner and outer damping zones, we damp the gas azimuthal and radial velocity, and in the outer zone, we damp the vertical dust velocity. We also damp the gas density in the entire domain back to the initial condition. Each damping happens on a dimensionless timescale of $T = 0.0316$. For the sake of shortness, we provide an overview of the boundary conditions in Appendix A.

Table 1. Initial setup values to study streaming instability in 2D

Parameter	Value
$\theta_{\text{min}}, \theta_{\text{max}}$	1.556796, 1.584796
$r_{\text{min}}, r_{\text{max}}$	9.3 au, 10.7 au
N_r, N_θ	4096, 1024
St	0.01
M_*	M_\odot
R_0	10 au
H_0/R	0.07
$H_{d,0}/R$	0.0014
η	0.0049
Π	0.07
Σ_0	390 g cm^{-2}
$\Sigma_{d,0}$	3.9 g cm^{-2} for $Z = 0.01$
$\Sigma_{d,0}$	7.8 g cm^{-2} for $Z = 0.02$
P	-1
Q	-1
T	$2\pi/\Omega_K(R = 1\text{au})$
τ_{SD}	$2\pi/\Omega_K(R = 1\text{au})$

Notes. The gas surface density Σ_0 was chosen such that the resulting midplane density at 10 au agrees well with the midplane density profiles in Fig. 4. We determine the initial value of η and Π with equation 5 in [Youdin & Johansen \(2007\)](#) and equation 3 in [Li & Youdin \(2021\)](#), respectively.

3. Results

One feature of streaming instability is strong clumping, which allows the disk to form clumps with higher density than the background ([Yang et al. 2017](#); [Li & Youdin 2021](#); [Lesur et al. 2023](#)). To be relevant for planet formation processes, these clumps must show densities around the Hill density, ρ_{Hill} , to collapse gravitationally. This section will investigate the ability to form these clumps for two surface density ratios ($Z = \Sigma_d/\Sigma_g = 0.01$, $Z = 0.02$). An overview of all relevant disk parameters is given in Table 1. Figure 1 shows the difference between two simulations after 100 orbits, each starting with one of the two aforementioned values. One can directly see that the higher surface density ratio leads to separated clumps.

3.1. Clump evolution with $Z = 0.02$

The disk with $Z = 0.02$ is evolved for 160 orbits to see the clump drifting behavior. In Fig. 2, we show the evolution of the surface density ratio Σ_d/Σ_g as a function of radial position and time as well as the 2D dust density at 160 orbits.

We indicate the theoretical radial drift due to a constant drift velocity of $v_{r,\text{clump}} = -30 \text{ cm s}^{-1}$ with a white line that we fitted by eye. In addition, we compare this clump drift velocity to the drift velocity of the background dust disk, $v_{r,\text{bg}}$, which we determine with equation 10 in [Birnstiel \(2024\)](#) which follows the solution by [Nakagawa et al. \(1986\)](#). We determine $\epsilon_{\text{bg}} \approx 0.5$ and $v_K - v_{\text{gas},\varphi} = \eta \cdot v_{\varphi,K} \approx 4680 \text{ cm s}^{-1}$ in the midplane at a position of 9.72 au after 100 orbits which yields a value of $v_{r,\text{bg}} \approx -41 \text{ cm s}^{-1}$. This comparison shows that due to the higher dust-to-gas ratio inside the formed clumps (up to $\epsilon \approx 6$), they drift inwards slower than the background dust disk.

The results for just a factor of 2 higher ratio of surface densities show that secondary clumping appears very early in the disk's evolution and the entire domain. This evolution agrees with [Li & Youdin \(2021\)](#) (see their Fig. 2, lower panel) despite their use of Lagrangian particles to model dust and local shearing box simulations. The question is whether the clump densities are high enough to be relevant for gravitational collapse by reaching the Hill density,

$$\rho_{\text{Hill}} = \frac{9 M_*}{4\pi R^3}, \quad (1)$$

with R the cylindrical distance to the star and M_* the mass of the central star (see appendix B of [Klahr & Schreiber 2020](#), also for the difference between Roche- and Hill density). To determine if the clump density is high enough, we plot in Fig. 3 the maximum density for the simulation with $Z = 0.02$ between 9.4 au and 10.4 au and compare it with the evolution of maximum dust density for the simulation with $Z=0.01$. We include a horizontal line at $\rho_{\text{dust,max}}/\rho_{\text{Hill}} = 1$.

The comparison indicates that with a dust-to-gas density ratio of $Z = 0.02$, the maximum density due to secondary clumping after 160 orbits is roughly 30% of the Hill density at 10 au. In addition, the evolution of the maximum dust density shows an exponential behavior over time once the streaming instability sets in. The maximum density is related to many clumps that alternate in having the highest density, and extrapolating this exponential behavior, reaching the Hill density would take roughly 480 orbits. To compare our results with those of local shearing box simulations, e.g., [Li & Youdin \(2021\)](#) or recently [Lim et al. \(2024b\)](#), we need to take into account that our value of the pressure gradient is 0.07 instead of the typically used value of 0.05. [Li & Youdin \(2021\)](#) provide with equation 9 a

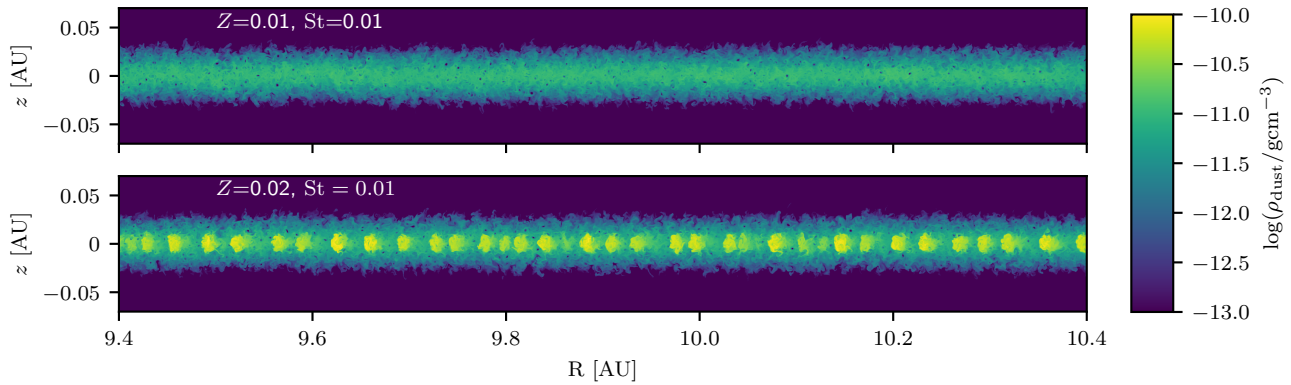


Fig. 1. Comparison between a dust fluid simulation with a metallicity of $Z=0.01$ (top) and $Z = 0.02$ (bottom) after 100 orbits at 10 au

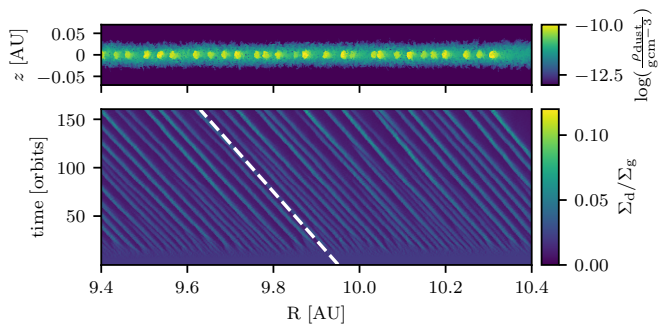


Fig. 2. Evolution of the disk with $\Sigma_d/\Sigma_g = 0.02$. Top: 2D dust density after 160 orbits, bottom: Evolution of the surface density ratio over 160 orbits. The white dashed line shows the theoretical radial drift with a constant drift velocity of $v_{r,\text{clump}} = 30 \text{ cm s}^{-1}$.

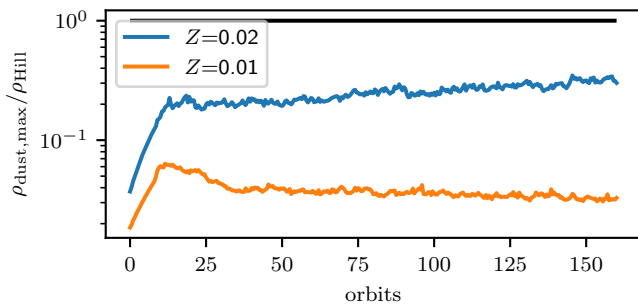


Fig. 3. Evolution of the maximum dust density between 9.4 and 10.4 au over 160 orbits for the considered simulations. The black line indicates the density ratio that clumps need to reach to collapse under their own gravity. The domain is chosen not to consider clumps that are an artifact from the outer boundary.

method to convert from $Z_{\text{crit}}(\text{St} = 0.01, \Pi = 0.05) \approx 0.016$ to $Z_{\text{crit}}(\text{St} = 0.01, \Pi = 0.07) \approx 0.022$. Because this value is slightly larger than our chosen value, we would not expect to be in the strong clumping region of the parameter space in Li & Youdin (2021) (from their Fig. 1). In Lim et al. (2024b) the value of $Z_{\text{crit}}(\text{St} = 0.01, \Pi = 0.05)$ is reduced to values < 0.01 due to higher resolution. Even with our pressure gradient, this would lead to $Z_{\text{crit}}(\text{St} = 0.01, \Pi = 0.07) < 0.014$ which is fulfilled in our simulation. Hence, with most recent local simulations running for much longer timescales, we expect to be in the strong collapsing part of their parameter space.

Investigating the spatial separation of clumps from Fig. 1 and 2 indicates that 33 clumps form within one au, leading to a separation of roughly 0.03 au. The gas scale height at 10 au is 0.7 au, resulting in a mean clump separation of $H_g/23$.

3.2. Comparison of disk midplane gas densities to critical Hill density

In the previous section, we mentioned that the critical Hill density for gravitational collapse only depends on the star's mass and the distance from the star, showing a substantial decrease with this distance. In contrast, the midplane gas density profiles can have different radial behaviors depending on the power-law index and the density at the characteristic scaling radius. These variations naturally occur due to different processes that dominate the disk evolution (Miotello et al. 2023). In this section, we want to compare five different midplane gas density profiles to their respective Hill density to see if and where sweet spots for planetesimal formation exist, i.e., where the ratio of Hill- to midplane density becomes sufficiently small.

Firstly, we use the recent constraints of disk parameters in Martire et al. (2024) for the four disks MWC 480, IM Lup, GM Aur, and HD 163296 by using the values from their stratified models. For each disk, we compute the profile of the gas surface density Σ_g , the midplane gas scale height H_g , the midplane gas density using $\rho_g = \Sigma_g / \sqrt{2\pi}H_g$ and the Hill density. The fifth midplane density is determined from the surface density profile of TW Hya, given in Yoshida et al. (2022), in combination with the scale height from Chiang & Goldreich (1997)

$$H_{\text{CG97}} = 0.045 \cdot R \cdot \left(\frac{R}{\text{au}}\right)^{2/7}, \quad (2)$$

which serves as an approximation for this almost face-on disk. The same gas scale height profile is used to determine the radial profile of the sound speed using $c_s = H_{\text{CG97}} \cdot \Omega_K$ for TW Hya. We approximate the gas angular velocity with the Keplerian angular velocity. The solid line indicates the radial domain in which the surface density profile was robustly determined. Yoshida et al. (2022) discussed that the true profile beyond five au needs to be smaller than the extrapolation to not become gravitationally unstable. For reference, we add the midplane gas density of our model at a location of 10 au. The comparison of these profiles to the Hill density is shown in Fig. 4.

Firstly, it should be pointed out that the profiles for four disks from Martire et al. (2024) define a narrow band that agrees well

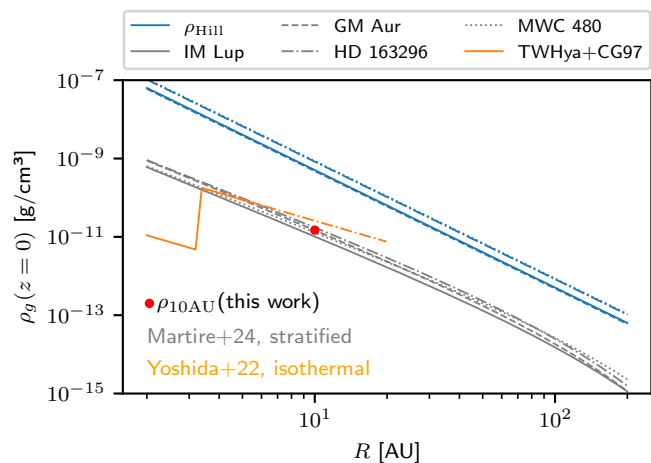


Fig. 4. Comparison between five midplane gas density profiles (grey) and their critical Hill densities (blue). For reference, the red dot indicates our work’s central location and gas density. A similar plot, though with only one gas density profile, was already shown in [Klahr & Schreiber \(2020\)](#).

with the profile of TW Hya for radii smaller than six au. Secondly, the Hill- to midplane gas density ratio decreases when the radius increases to roughly 50-60 au. For the disk IM Lup, the density ratio decreases from 50 at 10 au to 30 at 30 au. This suggests that the critical density is reached more easily outside 10 au.

4. Discussion

A massive disk with $Z = 0.02$, $\Sigma_g(10\text{au}) = 390 \text{ g/cm}^2$ and $H_g = 0.7 \text{ au}$ already produces denser dust concentrations after approximately 20 orbits. However, even after 160 orbits of evolution, these clumps only show a density of 30 % of the Hill density, and in total, 480 orbits would be necessary to reach this critical density by continuous growth. This suggests that the first gravitationally unstable clumps form early in the disk’s evolution. An important point to consider here is the fact that the four considered disks from [Martire et al. \(2024\)](#) are known as some of the most luminous disks observed so far and, therefore, may also be the heaviest ones. Less heavy disks will be more frequent, raising the question of how much time clumps need in these disks to become as dense as the Hill density. Rescaling our isothermal disk surface density with a factor of 6.5 to make it comparable to the disk in [Flock & Mignone \(2021\)](#) and extrapolating the maximum dust density shows that at least 1000 orbits are necessary to form dense enough clumps.

It should be mentioned that no theory yet predicts how the maximum local dust density evolves in time due to non-linear streaming instability. This is especially true for the strong clumping phase, where we find multiple clumps competing for the highest dust density. This means there is no unique function we can use to extrapolate the profile from Fig. 3. Our choice of an exponential profile is based on the fact that once the non-linear state of the instability sets in, producing the first filaments, the profile shows a linear behavior in the linear logarithmic plot. Hence, there is no guarantee that the profile will continue to be of exponential shape. Still, it might represent the process of filaments merging and existing clumps becoming denser with time.

On the other hand, when these clumps move inwards and grow in density, the radial drift becomes smaller as the dust shields itself from aerodynamic drag, creating a traffic jam. This

traffic jam allows the clumps to collect additional mass from larger radii. The distance of one au (approximately two au) traveled by the clumps in a massive (less massive/compact) disk during 480 (1000) orbits could then be seen as upper limits. Additional simulations with larger radial domains can be performed to verify the necessary number of orbits for reaching the Hill density and the small radial drift during this time, but this is outside the scope of this work.

In Sect. 3.1, we have shown that more dust-enriched clumps move inwards with a smaller velocity than the background dust disk. We expect these clumps to drift inwards even slower as they force the gas to rotate with Keplerian velocity when they grow in dust-to-gas ratio. However, why clumps do not slow more will be an open question for future projects.

A comparison of midplane density profiles for five disks with the Hill density (see Fig. 4) shows that the critical density tends to decrease faster with R than the disk profiles. This suggests that a sweet spot for dense enough clumps forming due to streaming instability might exist in the outer part of the disk where the critical density is closer to the gas midplane values. However, these sweet spots may be too far from the star, e.g., 50 au, such that orbital times are large and clump formation takes too long to be relevant.

In Sect. 3.1, we have mentioned that the separation of formed clumps at 10 au is much smaller than one au, and Fig. C.2 suggests that for a less massive or compact disk, only Band 1 of ALMA would be capable of showing good contrast between the optically thick clumps and the optically thin background. Because the resolution of ALMA is typically on the order of a few au, we can’t resolve the clump separation. The ngVLA will also observe at long wavelength (ALMA Band 3 and longer wavelength) with an estimated increase of baseline by an approximate factor of 10 (see [Ricci et al. 2018](#)). Even with a resolution of 1 au, the distance between the clumps will not be possible to resolve. However, [Scardoni et al. \(2024\)](#) introduces a method to detect unresolved dust rings in protoplanetary disks by using azimuthal brightness variations of inclined disks.

5. Conclusion

For the first time, we presented global dust-fluid models of streaming instability in stratified protoplanetary disks, which undergo a strong clumping phase. Using realistic density and temperature profiles, streaming instability sets in for a disk with a dust-to-gas ratio of $Z = 0.02$, and first clumps can be observed already after 20-25 orbits, confirming previous works. Investigating the maximum dust density of these clumps indicates that 30% of the Hill density can be reached after 160 orbits when considering massive disks like GM Aur, IM Lup, HD 163296, MWC 480, or TW Hya, which share astonishingly similar surface density profiles. Extrapolation suggests the maximum density to reach the critical Hill density within 480 orbits in which clumps drift only maximal one au. For less massive or compact disks, we find a factor of 2 increase in the necessary number of orbits as well as the distance that clumps drift inwards. We highlight that depending on the midplane dust density profile, the Hill density usually decreases faster than the fluid densities. This could make it possible to reach clump densities close to the critical density faster in the outer parts of the disk. Even though such clumps might already exist in observed protoplanetary disks, we could not resolve them with ALMA or the ngVLA due to their small spatial separation.

Acknowledgements. We thank Francesco Zagaria for the helpful discussion about recent constraints of disk parameters that led to the final version of Fig.

4. In addition, we want to thank the referee for the supportive report and suggestions to improve this work.

References

- Abod, C. P., Simon, J. B., Li, R., et al. 2019, *ApJ*, 883, 192
- Armitage, P. J. & Kley, W. 2019, *From Protoplanetary Disks to Planet Formation: Saas-Fee Advanced Course 45*. Swiss Society for Astrophysics and Astronomy
- Benítez-Llambay, P., Krapp, L., & Pessah, M. E. 2019, *ApJS*, 241, 25
- Benítez-Llambay, P. & Masset, F. S. 2016, *ApJS*, 223, 11
- Birnstiel, T. 2024, *ARA&A*, 62, 157
- Birnstiel, T., Dullemond, C. P., Zhu, Z., et al. 2018, *ApJ*, 869, L45
- Chiang, E. I. & Goldreich, P. 1997, *ApJ*, 490, 368
- de Val-Borro, M., Edgar, R. G., Artymowicz, P., et al. 2006, *MNRAS*, 370, 529
- Dominik, C., Min, M., & Tazaki, R. 2021, *OpTool: Command-line driven tool for creating complex dust opacities*, *Astrophysics Source Code Library*, record ascl:2104.010
- Dullemond, C. P., Ziampras, A., Ostertag, D., & Dominik, C. 2022, *A&A*, 668, A105
- Flock, M. & Mignone, A. 2021, *A&A*, 650, A119
- Gole, D. A., Simon, J. B., Li, R., Youdin, A. N., & Armitage, P. J. 2020, *ApJ*, 904, 132
- Johansen, A., Oishi, J. S., Mac Low, M.-M., et al. 2007, *Nature*, 448, 1022
- Johansen, A., Youdin, A., & Mac Low, M.-M. 2009, *ApJ*, 704, L75
- Klahr, H. & Schreiber, A. 2020, *ApJ*, 901, 54
- Kowalik, K., Hanasz, M., Wółtański, D., & Gawryszczak, A. 2013, *MNRAS*, 434, 1460
- Lesur, G., Flock, M., Ercolano, B., et al. 2023, in *Astronomical Society of the Pacific Conference Series*, Vol. 534, *Protostars and Planets VII*, ed. S. Inutsuka, Y. Aikawa, T. Muto, K. Tomida, & M. Tamura, 465
- Li, R. & Youdin, A. N. 2021, *ApJ*, 919, 107
- Lim, J., Simon, J. B., Li, R., et al. 2024a, *ApJ*, 969, 130
- Lim, J., Simon, J. B., Li, R., et al. 2024b, *arXiv e-prints*, arXiv:2410.17319
- Liu, H. & Bai, X.-N. 2023, *MNRAS*, 526, 80
- Martire, P., Longarini, C., Lodato, G., et al. 2024, *A&A*, 686, A9
- Miotello, A., Kamp, I., Birnstiel, T., Cleeves, L. C., & Kataoka, A. 2023, in *Astronomical Society of the Pacific Conference Series*, Vol. 534, *Protostars and Planets VII*, ed. S. Inutsuka, Y. Aikawa, T. Muto, K. Tomida, & M. Tamura, 501
- Nakagawa, Y., Sekiya, M., & Hayashi, C. 1986, *Icarus*, 67, 375
- Ricci, L., Isella, A., Andrews, S. M., et al. 2018, *arXiv e-prints*, arXiv:1803.04467
- Scardoni, C. E., Booth, R. A., & Clarke, C. J. 2021, *MNRAS*, 504, 1495
- Scardoni, C. E., Booth, R. A., Clarke, C. J., Rosotti, G. P., & Ribas, Á. 2024, *ApJ*, 970, 109
- Schäfer, U. & Johansen, A. 2022, *A&A*, 666, A98
- Schäfer, U., Johansen, A., & Banerjee, R. 2020, *A&A*, 635, A190
- Sekiya, M. & Onishi, I. K. 2018, *ApJ*, 860, 140
- Squire, J. & Hopkins, P. F. 2018, *MNRAS*, 477, 5011
- Weber, P., Pérez, S., Benítez-Llambay, P., et al. 2019, *ApJ*, 884, 178
- Woitke, P., Min, M., Pinte, C., et al. 2016, *A&A*, 586, A103
- Yang, C.-C. & Johansen, A. 2014, *ApJ*, 792, 86
- Yang, C.-C., Johansen, A., & Carrera, D. 2017, *A&A*, 606, A80
- Yoshida, T. C., Nomura, H., Tsukagoshi, T., Furuya, K., & Ueda, T. 2022, *ApJ*, 937, L14
- Youdin, A. & Johansen, A. 2007, *ApJ*, 662, 613
- Youdin, A. N. & Goodman, J. 2005, *ApJ*, 620, 459
- Ziampras, A., Sudarshan, P., Dullemond, C. P., et al. 2024, *MNRAS*[arXiv:2409.15420]

Appendix A: Boundary conditions

As boundary conditions for gas and dust, we proceed as follows: In the meridional direction, we use the central difference scheme to approximate the gas density gradient and use a simple forward Euler to extrapolate the density into the ghost cells. We do not allow inflow into the domain at the same boundary by setting the ghost cell values to 0 in case the velocity points into the domain. Using the same method, we also do not allow the inflow of material into the domain at the radial boundaries. Gas is only allowed to leave the domain. We use symmetrical boundary conditions for those components of the gas density and 3D velocity that are not explicitly specified, meaning that the ghost cell value is a copy of its corresponding value in the computational domain. For the dust density and the dust velocity components, we use symmetric boundary conditions in the radial and meridional directions but prevent dusty material from entering the domain in both dimensions using the same method as described for gas.

Appendix B: Damping and refilling in FARGO3D

Compared to the setup from [Flock & Mignone \(2021\)](#), we use a different equation to damp gas and dust variables close to the radial boundary conditions. The method is described in [de Val-Borro et al. \(2006\)](#). The equation that describes the damping of a variable $x(r, \theta, t)$ (e.g., the density of gas and dust and its velocity components) is

$$\frac{dx}{dt} = -\frac{x - x_0}{\tau_{SD}} \cdot W(r), \quad (\text{B.1})$$

where $x_0 = x(r, \theta, t=0)$ is the value at the initial conditions, τ_{SD} defines the timescale on which damping happens, and $W(r)$ defines a parabolic function which equals 1 at the boundary between ghost cells and computational domain (in which damping happens) and which equals 0 at the boundary between not damped and damped region within the computational domain. The numerical solution to Eq. B.1 is gained implicitly:

$$\frac{dx}{dt} \approx \frac{x^{n+1} - x^n}{\Delta t} = -(x^{n+1} - x_0) \cdot \frac{W(r)}{\tau_{SD}}. \quad (\text{B.2})$$

Rearranging for x^{n+1} and using $\tau_d = \frac{\tau_{SD}}{W(r)}$

$$x^{n+1} = \frac{x^n \cdot \tau_d + x_0 \cdot dt}{\tau_d + \Delta t}. \quad (\text{B.3})$$

For FARGO3D the expression of $W(r)$ is different for the inner damping-zone (in the following $W_{in}(r)$) and outer damping-zone (in the following $W_{out}(r)$)

$$W_{in}(r) = \left(\frac{r - r_{sup}}{r_{max} - r_{sup}} \right)^2, \quad W_{out}(r) = \left(\frac{r_{inf} - r}{r_{inf} - r_{min}} \right)^2, \quad (\text{B.4})$$

where r_{inf} (r_{sup}) is the spherical radius that defines the location of the inner (outer) damping zone. In [Flock & Mignone \(2021\)](#), they use a dimensionless value of $T = 1.0$ for the damping timescale where the characteristic radius of the disk is one au. We, however, use a characteristic radius of 10 au but want to use the same timescale for damping. This results in a dimensionless timescale of $\tau_{SD} = 0.0316$

Because dust will drift inwards due to the interaction with the gas, but dusty material is not allowed to enter the domain from outside, we use a similar artificial dust refilling method as described in [Flock & Mignone \(2021\)](#) to add dust in the outer

damping zone. In every time step, the dust density of each damping zone cell, ρ_d , is compared to the initial value $\rho_{d,0}$. If the density is found to be smaller than 25% of the initial value, we reset the density back to its initial value, e.g. $\rho_d = \rho_{d,0}$.

To prevent dust from accumulating at the inner damping zone, we use the same method as in [Flock & Mignone \(2021\)](#) and reduce the azimuthal dust velocity in every time step with $v_{d,\phi} = (1 - 10^{-8}) \cdot v_{d,\phi}$. This will slow down the dust in the azimuthal direction and increase its radial velocity.

In [Flock & Mignone \(2021\)](#), they use an additional gas damping in the entire domain to account for the fact that dust drags gas outside the domain, but gas cannot flow into the domain. No gas damping would result in a continuous reduction of the gas mass and affect dust dynamics. We determine the new value of the gas density $\rho(r, \theta)$ for each grid cell after a time step Δt via

$$\rho(r, \theta) = \rho_0(r, \theta) + [\rho((r, \theta), t) - \rho_0(r, \theta)] \cdot e^{2\Delta t/T}. \quad (\text{B.5})$$

For this damping technique, we also use a dimensionless timescale of $T = 0.0316$.

Appendix C: Observability of forming clumps

As boundary conditions for gas and dust, we proceed as follows: In the meridional direction, we use the central difference scheme to approximate the gas density gradient and use a simple forward Euler to extrapolate the density into the ghost cells. We do not allow inflow into the domain at the same boundary by setting the ghost cell values to 0 in case the velocity points into the domain. Using the same method, we also do not allow the inflow of material into the domain at the radial boundaries. Gas is only allowed to leave the domain. We use symmetrical boundary conditions for those components of the gas density and 3D velocity that are not explicitly specified, meaning that the ghost cell value is a copy of its corresponding value in the computational domain. For the dust density and the dust velocity components, we use symmetric boundary conditions in the radial and meridional directions but prevent dusty material from entering the domain in both dimensions using the same method as described for gas.

C.1. Dust opacities at ALMA band wavelengths

In Sect. 3, we have set our focus on five disks that are among the most luminous and probably the most massive disks. Even though these disks are easier to observe, they do not represent the typical disk population and their masses. Within this section, we set our focus to a more frequent disk type. As discussed in [Miotello et al. \(2023\)](#), a significant fraction of observed disks may consist of very compact disks with critical radii smaller than 15 au and high surface density in the inner region. In addition, they argue that no ALMA sample exists that allows entanglement between a radially extended, low-mass disk or a radially compact disk. Both scenarios allow us to consider a disk that shows a smaller surface density at 10 au than the value in Tab. 1. We will use the value specified in [Flock & Mignone \(2021\)](#), which can be obtained from our disk by a rescaling factor of 6.5.

To identify one or more suitable bands for observing formed clumps, we proceed as follows. We use three different dust grain composition models: The model described in [Dullemond et al. \(2022\)](#) (further referred to as D22), the DSHARP model described in [Birnstiel et al. \(2018\)](#), and the DIANA model from [Woitke et al. \(2016\)](#). For all models, we then use the publicly available tool *opTool* ([Dominik et al. 2021](#)) to compute the dust

opacity for absorption in a wavelength range of 0.05 - 9 mm. Because the material density due to the specified compositions varies, we receive different dust grain sizes at 10 au (see legend of Fig. C.1 for the resulting grain sizes), given a Stokes number of 0.01. Using the wavelength range of each ALMA band, we can compute the mean absorption opacity for each band. We also plot in black the dust absorption opacity for the default grain size distribution of opTool between 0.05 and 3000 μm , assuming a power-law index of -3.5 and a grain composition purely by pyroxene.

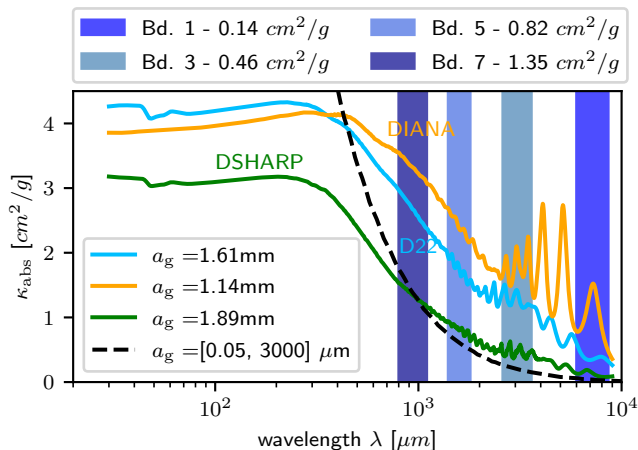


Fig. C.1. Dust absorption opacities using the dust grain compositions DSHARP (Birnstiel et al. (2018)), DIANA (Woitke et al. (2016)) and the composition mentioned in Dullemond et al. (2022) (referred to as D22 in the plot). The black dashed line shows the absorption opacity for the default opTool grain size distribution and each grain consisting purely of pyroxene. The vertical bars indicate the wavelength range of different ALMA bands. The mean absorption opacity for each band is calculated based on the DSHARP composition.

C.2. Optical depth profile of forming clumps

The remaining question is whether these clumps can be observed in protoplanetary disks. The ideal scenario is to use, for instance, ALMA with a band in which the clumps are optically thick, but the dust disk around the clumps is optically thin. For further analysis, we stick to the DSHARP model from Birnstiel et al. (2018) as it leads to the smallest opacities compared to the DIANA model (Woitke et al. 2016) and the model described in Dullemond et al. (2022) (See Fig. C.1 for comparing the three models). To show the range in optical depth for suitable ALMA bands (Band 1 to 7) we use the mean absorption opacity for Band 1 ($\kappa_{\text{Band1}} = 0.14 \text{ cm}^2 \text{ g}^{-1}$) and Band 7 ($\kappa_{\text{Band7}} = 1.35 \text{ cm}^2 \text{ g}^{-1}$), multiply these values with the dust surface density of the considered disk and show the results in Fig. C.2. The area between both optical depth profiles, relevant for intermediate ALMA bands, is shown in grey. Using the profile from Band 1 shows that the clumps typically have values around 0.3-0.5, while the regions around the clumps are below 0.1. The effect of streaming instability to reduce the surface density of the background disk and, therefore, its optical depth was already mentioned in Scardoni et al. (2021). They showed that when the streaming instability leads to optically thick clumps, the simulated fluxes in mm wavelength range are consistent with those observed from real disks.

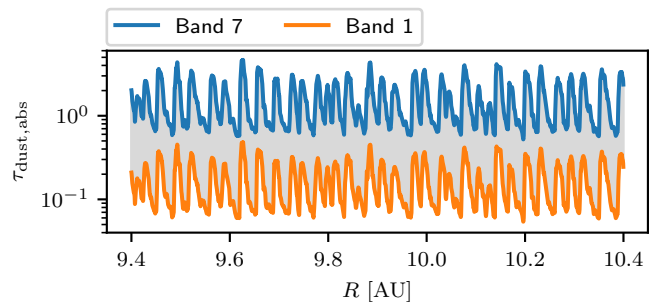


Fig. C.2. Dust optical depth after 100 orbits as a function of radius for the simulation with $Z = 0.02$. The disk we consider here is gained by rescaling the density from the simulation in Fig. 2 by a factor of 6.5. The grey region between both curves indicates the possible values of optical depth that are relevant for observations between Band 1 and Band 7.